Self-Compensation in Transparent Conducting F-doped SnO_2

Jack E. N. Swallow,[†] Ben Williamson,[‡,¶] Thomas J. Whittles,[†] Max Birkett,[†] Thomas J. Featherstone,[†] Nianhua Peng,[§] Alex Abbott,[‖] Mark Farnworth,[‖] Kieran J. Cheetham,[‖] Paul Warren,[‖] David O. Scanlon,[‡,¶,⊥] Vin R. Dhanak,[†] and Tim D. Veal[*,†]

†*Stephenson Institute for Renewable Energy and Department of Physics, University of Liverpool, Liverpool L69 7ZF, United Kingdom*

‡*Department of Chemistry, University College London, Kathleen Lonsdale Materials Chemistry, 20 Gordon Street, London WC1H 0AJ, United Kingdom*

¶*Thomas Young Centre, University College London, Gower Street, London WC1E 6BT, United Kingdom*

§*Surrey Ion Beam Centre, University of Surrey, Surrey GU2 7XH, United Kingdom*

‖*NSG Group, European Technical Centre, Hall Lane, Lathom, Ormskirk, Lancashire, L40 5UF, United Kingdom*

⊥*Diamond Light Source Ltd., Diamond House, Harwell Science and Innovation Campus, Didcot, Oxfordshire OX11 0DE, United Kingdom*

E-mail: T.Veal@liverpool.ac.uk

Table of Contents Figure and Summary

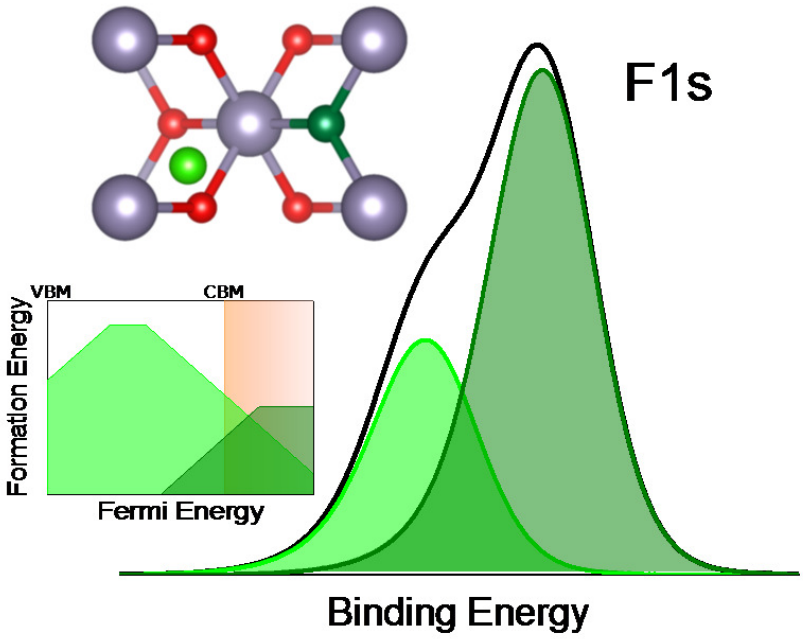

Compensating acceptor defects dramatically reduce electronic performance of $F:SnO_2$ transparent conductor grown by chemical vapour deposition. Electron carrier mobilities are seen to be greatly diminished from the theoretically predicted optimum, and through implementing hybrid density functional theory calculations and experimental methods and analysis the defect responsible for self-compensation in $F:SnO_2$ is determined to be the fluorine interstitial.

Abstract

The factors limiting the conductivity of fluorine-doped tin dioxide (FTO) produced via atmospheric pressure chemical vapour deposition (APCVD) are investigated. Modelling of the transport properties indicates that the measured Hall effect mobilities are far below the theoretical ionized impurity scattering limit. Significant compensation of donors by acceptors is present with a compensation ratio of 0.5, indicating that for every two donors there is approximately one acceptor. Hybrid density functional theory calculations of defect and impurity formation energies indicate the most probable acceptor-type defects. The fluorine interstitial defect has the lowest formation energy in the degenerate regime of FTO. Fluorine interstitials act as singly charged acceptors at the high Fermi levels corresponding to degenerately n-type films. X-ray photoemission spectroscopy of the fluorine impurities is consistent with the presence of substitutional F_O donors and interstitial F_i in a roughly 2:1 ratio in agreement with the compensation ratio indicated by the transport modelling. Quantitative analysis through Hall effect, x-ray photoemission spectroscopy, and calibrated secondary ion mass spectrometry further supports the presence of compensating fluorine-related defects.

Introduction

Transparent conducting oxides (TCOs) are materials that combine the usually mutually exclusive properties of optical transparency and electrical conductivity.[1–3] This unique characteristic has led to the incorporation of TCOs into a number of modern technologies including low emissivity windows, solar cells, touch screens, and flat panel displays.[4–7] Currently, a very limited number of TCO materials dominate the consumer market. An example of this is the market for energy efficient windows which is led by fluorine-doped tin dioxide (FTO), a material that displays competitive opto-electronic properties to one of the industry leaders, tin-doped indium oxide (ITO), but offers higher chemical, mechanical and thermal resistance and can be deposited very cost effectively.[8,9]

FTO is a TCO consisting of a stannic oxide (SnO_2) framework with heavy donor incorporation of the fluorine dopant, maintaining a rutile structure.[10,11] A number of thin-film deposition methods are regularly used to prepare FTO, including spray pyrolysis,[12] chemical vapour deposition,[13] pulsed laser deposition,[14] and magnetron sputtering.[15] Commercial FTO is most commonly deposited via atmospheric pressure chemical vapour deposition (APCVD) in an on-line coating process where the manufacturing of the glass substrate and deposition of the TCO films are performed in a continuous process. An example of these products is the NSG TEC™ glass range.[16]

FTO possesses a fundamental electronic direct band gap of E_g=3.6 eV,[17,18] and an optical band gap that can often exceed 4 eV depending on the level of fluorine incorporation.[14,19] This contributes to achieve optical transmission of light in the visible region commonly around 80%.[20] In these materials it is generally assumed that fluorine acts as a substitutional, singly-charged donor occupying an oxygen site. This is often assumed because oxygen and fluorine have nearly the same atomic radii and similar bond energies with tin which should assist in fluorine being easily incorporated into the material.[11,21] Fluorine-doping of tin dioxide can result in very low resistivity FTO films, regularly less than 4×10^{-4} Ωcm.[16,22,23]

Naïvely, it is expected that the more fluorine atoms that are incorporated into the tin dioxide matrix, the more free electrons become available for conduction.[11] If this is the case, the amount of fluorine incorporated is only limited by the trade-off between optical and electrical properties - as the carrier density is increased, there is a corresponding increase in conduction electron plasma frequency and associated plasma reflectivity that limits the infrared transparency.[24–26] However, one interesting observation reported many times over the years is that the resistivity of FTO will initially decrease as carrier concentration increases and then begin to increase when carrier concentrations become sufficiently large.[22,27–31] While the initial decrease in resistivity is relatively simple to explain, being due to the extra free carriers contributing to conduction introduced into the material by the fluorine dopant, the origin of the eventual increase in resistivity at high doping levels is a much more debated

issue. A number of phenomena have been suggested, with a general underlying theme of the fluorine interstitial playing a major role.[10,11,29] However, only very limited evidence is available supporting this claim, mainly based on x-ray diffraction studies.[27–29,32,33]

In this study we use a combination of Hall effect measurements and modelling, and theoretical calculations based on density functional theory (DFT) to determine the factors limiting the carrier mobility in APCVD-deposited FTO films on soda lime glass. This information is then related to quantitative chemical analysis using x-ray photoemission spectroscopy (XPS) backed by secondary ion mass spectrometry (SIMS). These results point to a self-compensation mechanism occurring in FTO at high doping levels. With the aid of DFT formation energy calculations and XPS results we are able to infer the likely defect species.

Results and discussion

Transport Mobility

Transport mobilities of the FTO samples as a function of carrier concentration, as measured primarily by Hall effect, are shown in figure 1. For degenerately doped semiconductors, such as transparent conducting oxides, the dominant carrier scattering/mobility reducing mechanism in the majority of cases is ionised impurity scattering.[34,35] To simulate this effect, the degenerate form of the Brooks-Herring formula[36,37] has been implemented, labelled ionized impurity (II) in figure 1. All donors are assumed to be ionized and have a charge state of $Z_D = 1$, corresponding to substitutional fluorine, F_O. Other scattering mechanisms have been taken into account and are shown in figure 1. These are acoustic deformation potential (ADP),[38,39] longitudinal polar-optic phonons (LPO) (we use here the formalism set out by Low and Pines[40] and adapted by Fonstad and Rediker for SnO_2,[38] however a number of other approaches do exist[41,42]) and grain boundary scattering for both degenerate[43] (IG(Deg)) and non-degenerate[44] (IG) systems. The effects of neutral impurities, and other phonon effects were found to be negligible.

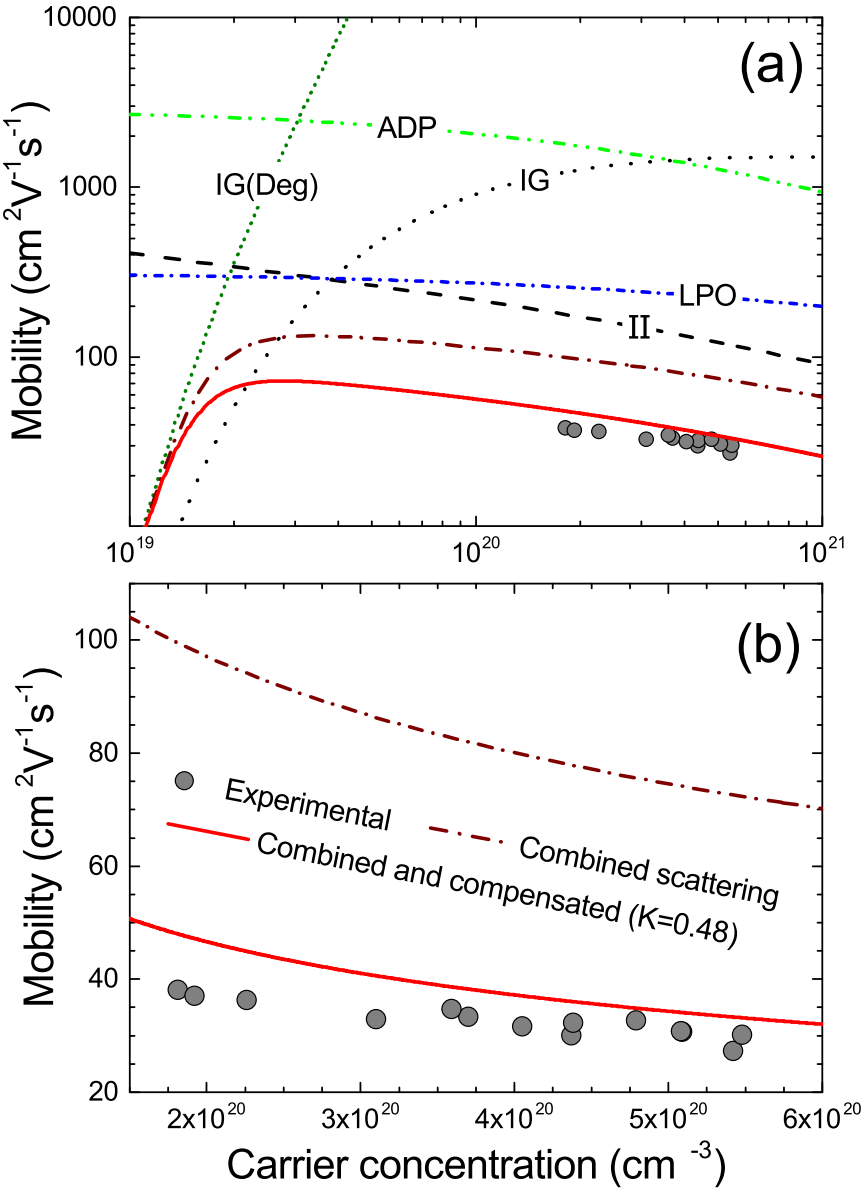

Figure 1: Transport data and Simulation for Hall mobility versus carrier concentration of FTO. (a) displays all theoretical curves calculated over a wide carrier concentration range whilst (b) shows only the combined theoretical model, the effect of compensation and the experimental data over the carrier concentration range relevant to the data. Model curves of dominant scattering mechanisms result from successive addition via Matthiessen's rule. The scattering mechanisms displayed are longitudinal polar-optical (LPO), acoustic deformation potential (ADP), grain boundary for both the degenerate (IG(Deg)) and non-degenerate case (IG), ionized impurity (II), and the effect due to compensation in the system.

Individual carrier scattering mechanisms are modelled and displayed in Figure 1 along with the combined transport mobility calculated according to Matthiessen's rule. This ap-

proach assumes the scattering mechanisms are independent of each other. All curves have been calculated using a band-edge effective mass of $m_r = 0.27m_0$[45] and a relative static dielectric constant of $\varepsilon(0) = 12.2$.[46] The band-edge effective mass and dielectric constants are assumed to be isotropic for these polycrystalline films.[38] The non-parabolicity of the conduction band was also accounted for using a carrier density-dependent effective mass.[47]

As shown in Figure 1, ionized impurity scattering becomes the dominant mobility limiting mechanism in SnO_2 above a carrier density of $\sim 5 \times 10^{19}$ cm^{-3}. This holds well with the predictions made by Martinez *et al.*[48] Our data points reside well above this threshold, indicating the heavily limiting effects of grain boundaries are negligible for our films. However, even in this regime the theoretical mobilities calculated are roughly three times higher than those measured. This relationship is supported by the modelling of temperature dependent Hall effect which can be seen in supporting information Figure S1. The results agree well with the work of Haitjema *et al.*[49] who suggest their calculated theoretical mobility is four times greater than that found experimentally. We attribute this to the effects of self-compensation in these samples. Self-compensation arises by the formation of acceptor defects that counter the dopant impurity properties.[35] The effects of self-compensation can be included in the transport model utilising a factor termed the 'compensation ratio' ($K = \frac{N_A}{N_D}$), which is simply defined as the ratio of the number of acceptors to donors present in the material.[50] This modifies the mobility limit due to ionized impurities as $\mu_{II} = \mu_{II}(0)\frac{Z_D - Z_A K}{Z_D^2 + Z_A^2 K}$ where $\mu_{II}(0)$ is the unattenuated ionized impurity mobility limit and Z_D and Z_A are the charge state of donors and acceptors respectively.[51] If we assume the charge state of the acceptor defect to be $Z_A = 1$, this equation reduces to $\mu_{II} = \mu_{II}(0)\frac{1-K}{1+K}$. Incorporating the compensation ratio into the model fit (the brown dash-dot curve labeled combined scattering in figure 1) we determine the level of compensation for a singly charged acceptor to be $K \sim 0.48$.

Theoretical Prediction of Defects

Hybrid density functional theory calculations have been performed to determine the formation energies of a range of likely intrinsic and extrinsic defects states in tin dioxide as a function of the Fermi level position. The defect species considered in this study are substitutional fluorine (F_O), interstitial fluorine (F_i), a fluorine substitutional-interstitial pair ($[F\text{-}F]_O$) together with the dominant intrinsic donor and acceptor defects in SnO_2 such as the oxygen vacancy (V_O) and the tin vacancy (V_{Sn}). All of these defects are displayed in Figure 2 for both *Sn-Rich/O-Poor* (left) and *Sn-Poor/O-Rich* (right) which are at the 'extremes' of the chemical potentials, i.e the formation of Sn metal under *Sn-Rich/O-Poor* conditions and O_2 gas under Sn-poor/O-rich conditions and thus the experimental situation is expected to lie somewhere between these two regimes. In each plot the valence band maximum (VBM) is set to $E_F = 0\,\text{eV}$ and the onset of degeneracy occurs from the conduction band minimum ($E_F = 3.6\,\text{eV}$) indicated by the graded orange area.

Under both growth regimes the oxygen vacancy (V_O) acts as the lowest formation energy intrinsic donor, behaving as a 'deep' defect with a negative-U behavior (the 2+/0 transition level occurs $\sim 0.76\,\text{eV}$ below the conduction band minimum (CBM)) meaning that V_O is unlikely to be a source of conductivity in SnO_2 which has been seen in previous theory[52–54] and experimental[55] studies alike. Oxygen vacancies have been identified as the intrinsic defect present in undoped TCOs such as In_2O_3, ZnO and SnO_2 via positron annihilation spectroscopy.[56] The neutral charge state for the tin vacancy (V_{Sn}) in each of the growth regimes has a very high formation energy and thus will not form or will form in negligible quantities. Under conditions which favour *p*-type defects (*Sn-Poor/O-Rich*) where the formation energy is $\sim$8.37 eV. This defect lies *ultra* deep in the band gap where the 0/1- lies $\sim 1.75\,\text{eV}$ above the VBM.

Under *Sn-Rich/O-poor* conditions substitutional fluorine (F_O) is the lowest formation energy donor and is *shallow* with the 1+/0 transition occuring $\sim 0.76\,\text{eV}$ above the CBM and the 0/1- level occuring $\sim 2.09\,\text{eV}$ above the CBM. Figure 3a displays the partial charge

density of F_O in the neutral charge state (F_O^0) showing the delocalisation of electron density in the conduction band, consistent with the resonant nature of substitutional F. There is also negligible distortion to the SnO_2 lattice as shown in Figure 3a giving rise to the low formation energy of F_O. The 1- charge state in this case does not act as an acceptor but the extra electron is instead donated to the conduction band. Interstitial fluorine (F_i) was found in our calculations to distort from the 'perfect' interstitial site towards a lattice oxygen site causing a displacement of the oxygen (Figure 3b). Figure 3b also shows that the electron density is highly localised in a *p*-orbital on the F_i and on the two opposing O *p*-orbitals, thereby trapping charge. This defect was found to be a *very* deep donor state as the $1+/0$ transition occurs $\sim$2.30 eV below the CBM. At Fermi energies above the CBM, V_{Sn} begins to compensate F_O ($\sim$1.7 eV above the CBM) thus negating the extra electrons and trapping the Fermi level at this point. Another species, the fluorine substitutional-interstitial pair which have been postulated theoretically at high concentrations and seen experimentally via simple changes in lattice parameters has also been calculated alongside F_O and F_i.[29,32,57] The $[F\text{-}F]_O$ defect possesses a relatively high formation energy and acts as an ultra deep donor with the $1+/0$ charge state lying 3.2 eV below the CBM.

Under *Sn-Poor/O-Rich* conditions, the formation energy of F_O is raised and those of F_i and V_{Sn} are lowered. Under these conditions, the F_i^- and F_O^+ defect states cross at $\sim$0.03 eV above the CBM trapping the Fermi energy at this point; this 'self-compensation' mechanism has been seen to occur in anatase TiO_2 also.[58] At higher Fermi energies, V_{Sn}^{4-} crosses the F_O^+ line at $\sim$0.23 eV above the CBM potentially causing further compensation. The formation energies of the $[F\text{-}F]_O$ defect charge states remain the same over the chemical potential range and the neutral charge state occurs at a lower formation energy than F_O under *Sn-poor/O-rich* conditions.

The middle plot in Figure 2 represents the realistic growth conditions under APCVD at a temperature of $\sim$900 K and a pressure of 1 atm. These conditions lie somewhere between the extremes of the chemical potentials discussed previously and as such, the defect landscape

transitions accordingly. The crossing point of the F_O^+ and F_i^- defect states now occurs at $\sim 0.55\,\mathrm{eV}$ above the CBM (shown by the dashed black line at E_F=4.15 eV) and above this point, compensation occurs.

In addition to the DFT calculations, we have calculated the partial charge densities for both the F_O^+ and the F_O^- defect charge states. Here it is shown that the electron density is delocalised when the F substitutes an oxygen and is localised when F is in an interstitial position. F_i^- also displays the relatively sizeable lattice distortion caused by the localisation of two electrons on the F atom and two adjacent O atoms. This depicts interstitial F as a deep acceptor (F_i^-), leading to the decrease in mobility seen when self-compensation occurs for a Fermi level of ∼4.1eV above the valence band maximum.

The inset of Figure 4 shows the absorption coefficient, α, which is calculated from the transmission data and film thickness. The optical gap is determined to be 4.2 eV from linear extrapolation of α^2 versus photon energy. Accounting for the valence band dispersion, the Fermi level is found to be $E_F = 4.1\,\mathrm{eV}$ above the valence band maximum (VBM) corresponding to the point where F_O^+ begins to be compensated by F_i^- which is in excellent agreement with the theoretically calculated value of 4.15 eV at 900 K, 1 atm. The charge state of F_i in this regime is $Z_A = -1$, justifying the initial assumption applied in the transport model and the compensation ratio of $K = 0.48$.

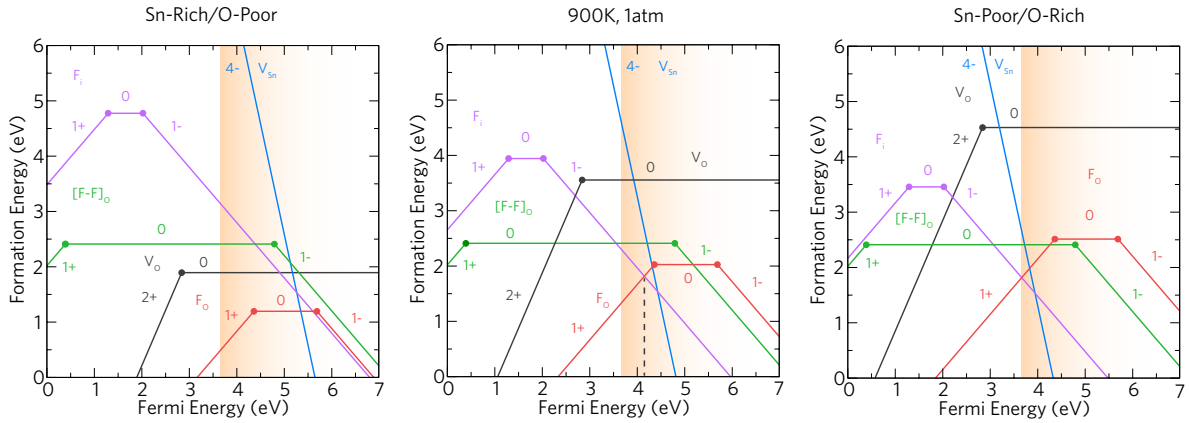

Figure 2: The calculated formation energies as a function of Fermi level position for *Sn-Rich/O-Poor* (left), at 900 K and 1 atm (middle) and *Sn-Poor/O-Rich* (right) growth conditions. In each regime the VBM is set at 0 eV and the conduction band is denoted by the orange area with the CBM at 3.6 eV. The dashed black line shown in the middle plot (900 K, 1 atm) represents the Fermi energy at the point where the F_O^+ and F_i^- lines cross. The solid dots indicate the transition levels from charge state q to q′, ϵ(q/q′).

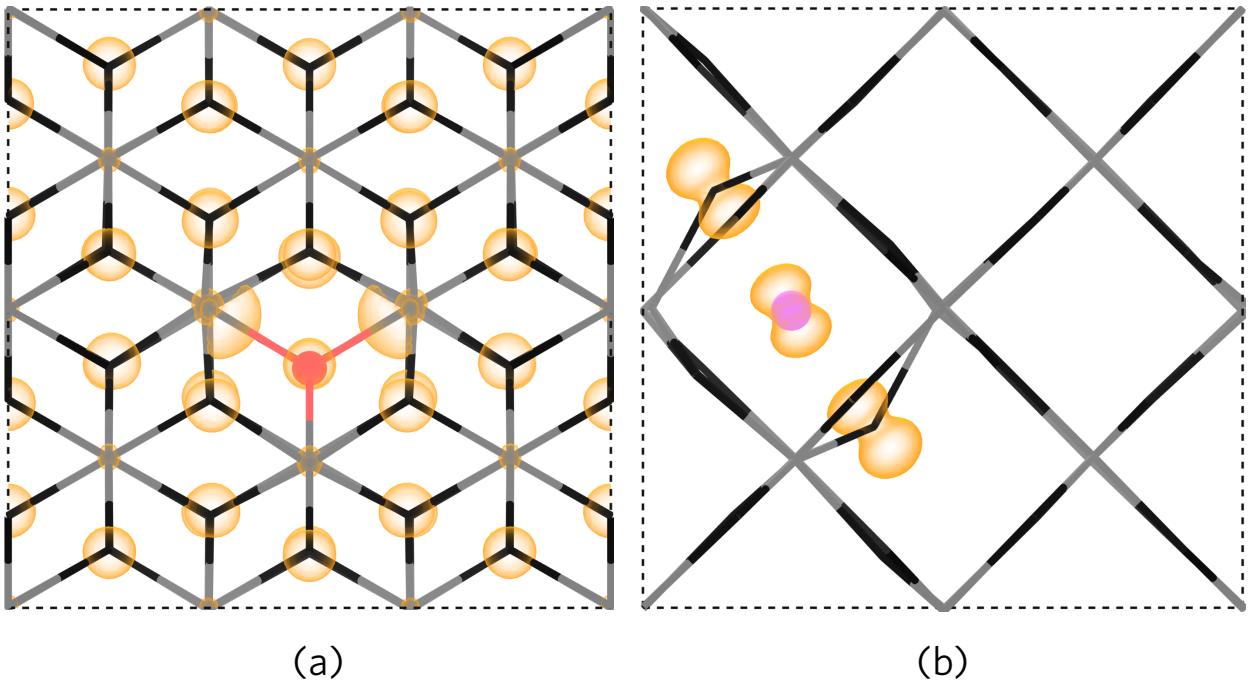

Figure 3: The calculated partial charge densities of (a) F_O^+ and (b) F_i^- down the {010} and {001} directions respectively. The Sn (grey) and O (black) atoms are depicted using a stick model for clarity, whilst the F atoms are coloured red (F_O) and pink (F_i) corresponding to the defect colour used in Figure 2. Charge densities of 0.001 eVÅ^{-1} and 0.02 eVÅ^{-1} were used for (a) and (b) respectively.

Core-Level XPS and Optical Reflectivity

In order to probe experimentally for evidence of F_i, high-resolution core-level XPS spectra of the Sn $3d_{5/2}$, O 1s and F 1s regions were recorded for degenerately doped FTO (n= 4.27×10^{20} cm^{-3}). All of these spectra were recorded after a low energy Ar^+ sputter to remove surface contamination. The level of contamination was monitored by taking survey spectra between sputter cycles. A noticeable reduction of a high binding energy component of the F 1s was also observed after sputtering (see Figure S3 in the supporting information for fitting of pre-sputtered FTO). We attribute this to surface contamination associated with fluorine bonded to carbon, consistent with the large shift to higher binding energy seen for fluorocarbon species elsewhere.[59–61]

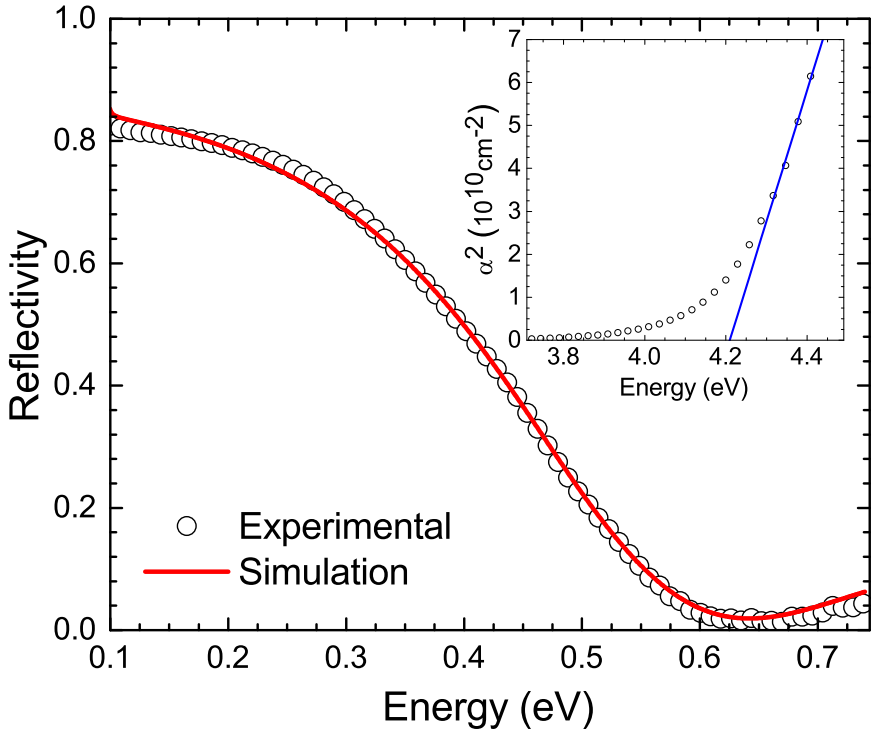

Figure 4: IR reflectivity data (circles) and optical model simulation (solid line) of FTO ($n = 4.27 \times 10^{20}cm^{-3}$) deposited on a glass/$SnO_2$/$SiO_2$ substrate. The inset plot displays optical absorption data with a linear extrapolation estimating the absorption onset. This shows an optical gap of 4.21 eV, corresponding to a Fermi level position 4.10 eV above the VBM.

Heavily-doped wide band-gap semiconductors such as TCOs display almost metallic-like

properties in the sense that they possess a large density of free carriers. This needs to be considered in the fitting of the core-level spectra, but is often ignored. At the high doping levels ($n > 10^{20}\text{cm}^{-3}$) present in our samples, plasmon loss features are commonly observed which manifest as a high binding energy component, representing the fraction of photoelectrons that have lost energy to the collective excitations of the free electron gas during photoemission from the material. However, interpreting these loss peaks in XPS is notoriously difficult due to their complex nature, with many different approaches having been employed.[62]

Here we employ the fitting procedure of Egdell *et al.*[63,64] who base their analysis on the Kotani-Toyazawa screening model.[65] A comprehensive discussion regarding the merits and drawbacks surrounding this approach can be found elsewhere.[66,67] Using this approach, both the Sn $3d_{5/2}$ and O 1s core-level peaks (figure 5) are fitted using two symmetric Voigt functions, one component at lower binding energy for the photoelectrons with no energy loss to plasmons, and plasmon-loss component at higher binding energy. A Shirley background is also used in the fitting.[68]

In order to achieve a meaningful fit to the data, the energy separation between the plasmon loss peak and the no loss component is required. This separation is determined by the free carrier plasmon frequency. The surface plasmon frequency can be determined from high resolution electron energy loss spectroscopy (HREELS) and dielectric theory simulations,[69,70] or the bulk plasmon frequency from infra-red reflectivity measurements and modelling.[71] IR reflectivity spectra of the FTO ($\text{n} = 4.27 \times 10^{20}$ cm^{-3}) is displayed in figure 4.

The transfer matrix method-simulated reflectivity spectrum seen in figure 4 allows for the determination of the plasmon energy ω_p. The extracted plasmon energy is $\omega_p = 0.50$ eV. The equation for the plasmon energy is given as $\omega_p = \sqrt{\frac{ne^2}{m^*\varepsilon_0\varepsilon(\infty)}}$ with the surface plasmon energy varying only by a factor of $\sqrt{\frac{\varepsilon(\infty)}{\varepsilon(\infty)+1}}$. Using a relative high frequency dielectric constant of 3.9, this results in a surface plasmon energy of $\omega_{sp} = 0.45$ eV as determined from the simulated plasmon energy. As emitted photoelectrons originate from up to 10 nm from the surface,

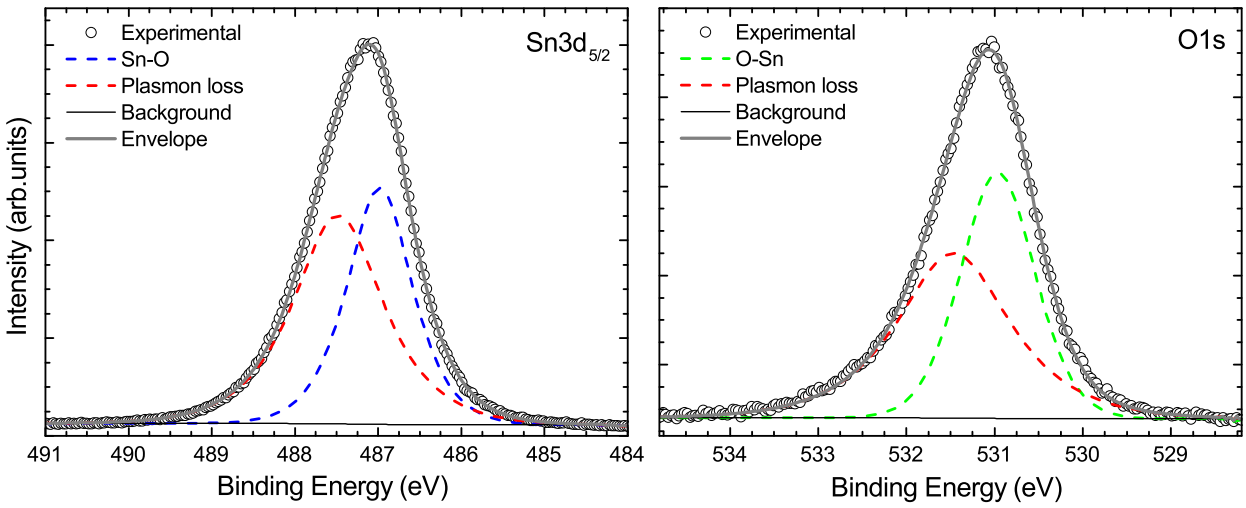

Figure 5: XPS spectra of the $Sn3d_{5/2}$ and O1s core levels of FTO (n= 4.27×10^{20}cm^{-3}) measured after argon plasma sputtering to remove surface contaminants. Two peaks are used to fit the data in each spectrum, a low binding energy component representing the un-attenuated peak and a high binding energy component representing the energy loss of the core-level to the collective free carrier gas.

the separation between screened and unscreened components is expected to lie in the region of 0.45 eV $\leq \Delta E_p \leq$ 0.50 eV.

Utilising this information, the fitting procedure for the Sn $3d_{5/2}$ and O $1s$ core levels in figure 5 involved simply constraining the no loss peak to plasmon loss peak energy separation to the determined plasmon energy range and allowing parameters to be optimised in the fitting procedure in order to achieve the best least squares fit. As can be seen from figure 5 there is excellent agreement between the fit and the experimental data. Both the Sn $3d_{5/2}$ and O1s peaks display sizeable plasmon loss components at 0.5 eV higher than the no loss peak. attenuated peaks are situated at 486.9eV and 530.9eV for Sn $3d_{5/2}$ and O $1s$ respectively, in good aggreement with other reported binding energy values.[48,72,73]

The full width at half maximum (FWHM) of the core-line components for the Sn and O are both under 1.0 eV. The full-widths of the high-binding energy components are broader than this owing to the finite plasmon lifetime broadening which has to be considered in addition to the natural line width and instrumental broadening of the core level peak. The plasmon loss peaks display greater Lorentzian character than the low binding energy peaks.

It is evident when the plasmon loss mechanism is accounted for in the XPS fitting that only a single Sn-O chemical environment can be discerned in the Sn $3d_{5/2}$ and O $1s$ spectra. This is expected given the bonding structure of SnO_2. Whilst a Sn-F bond peak could be expected in the Sn $3d_{5/2}$, the fluorine content in these samples is extremely low and so we can not distinguish it here in the presence of the strong Sn-O signal. The asymmetric peak shape of the tin and oxygen regions are commonly seen in reports on FTO,[20,22,74–76] although they are very rarely associated with plasmon loss events taking place.

We now turn our attention to the F $1s$ core level region and employ the same constraints applied to the Sn $3d_{5/2}$ and O $1s$ core levels, the data for which is shown in figure 6. A much reduced fluorocarbon species is still present, which is likely a result of the low sputtering energy used (as not to damage the structure of the FTO) not fully removing the surface carbon, although carbon incorporation into the bulk cannot be ruled out. Taking this into account, a single no loss core-level peak and associated plasmon loss peak pair (and additional high binding energy contaminant peak) provided an extremely poor fit to the data. The shoulder component could not be fit well under these constraints. This suggests there is another species of fluorine present within the material, in addition to the expected substitutional fluorine. In order to fit the F $1s$ spectra with two fluorine species present, a similar fitting procedure was used to that of the Sn $3d$ and O $1s$ core-levels. However, in the case of the fluorine we acknowledge that both fluorine core-lines will produce plasmon loss features and in fact we can further constrain the area ratios of the loss feature to its corresponding core-line because electrons originating from these two fluorine species will experience the same screening from the free electron gas. Carbon at the surface will not have an associated plasmon loss as electrons originating from the surface will not interact with the free electron gas in the bulk.

The loss features are again constrained to $\omega_{sp} \leq \Delta E_p \leq \omega_p$ from the respective core-line peaks. The substitutional peak and the peak labeled interstitial F in figure 6 are constrained to have the same FWHM as each other. The two loss peaks are constrained to have the same

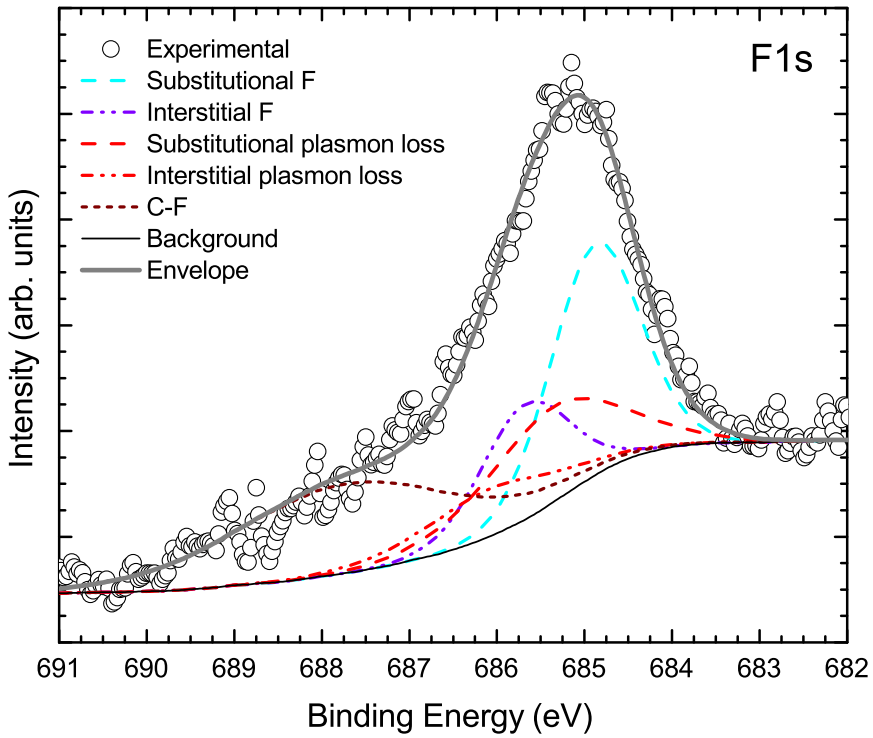

Figure 6: XPS spectra for the F 1s core level of FTO (n= 4.27×10^{20}cm^{-3}) measured after argon plasma sputtering to remove surface contaminants. Four peaks were used to fit the data representing substitutional fluorine (F_O), interstitial fluorine (F_i), and two further symmetric peaks representing the energy loss of each of the core levels to the collective free carrier gas. Additionally a small fluorocarbon species is seen at higher energy.

FWHM as each other, but it is allowed to differ from that of the no loss components. The binding energy positions of the substitutional and interstitial peaks are determined to be 684.9eV and 685.7eV respectively (see Table S1 in supporting information for a comparison to binding energies in the literature). As expected, the loss peaks take on a more Lorentzian character with a larger FWHM than the other components. The fitting is again in good agreement with the data. Multiple data sets from a range of FTO coatings with varying fluorine content have been fitted using the same fitting parameters and procedure. The fitting parameters for the XPS data from these other coatings are consistent with the ones from the spectra shown (see Figure S4 in supporting information).

The peak areas of the substitutional and interstitial F 1s peaks are extracted from the fit and the ratio of the two calculated. This ratio for this particular sample is found to be $\frac{A_{int}}{A_{sub}} =$

0.47. For six samples analyzed with 1.8×10^{20} cm^{-3} $< n <$ 5.5×10^{20} cm^{-3}, this peak area ratio is found to lie in the range 0.47 to 0.53 (see Figure S4 in the supplementary information). The peak areas are representative of the concentration of the given species of the material present in the sample, and hence we can deduce the fraction of the fluorine interstitial is $\sim$0.5 of the substitutional fluorine incorporated into the material. This ratio is remarkably close to the compensation ratio of $K = \frac{N_A}{N_D} = 0.48$ found from transport modelling in Fig. 1. Therefore, the experimental XPS evidence strongly supports the hypothesis of a compensating defect, and is consistent with the proposed defect of the fluorine interstitial determined as the lowest formation energy compensating defect by the DFT.

The fluorine interstitial acting as a singly charged compensating acceptor has been a well established hypothesis[11,27,28,32,57] for FTO, with researchers even providing similar evidence from XPS measurements such as Suffner *et al.*[29] on FTO nanoparticles. However, Suffner *et al.* did not include the effects of plasmon losses in their fitting and no transport properties of the material were reported. To our knowledge, nobody has yet made the connection, quantitatively or otherwise, between the transport compensation behaviour and the XPS chemical analysis that we have performed for FTO in this work. In addition to this, the DFT defect chemistry analysis has been clearly instructive in both the transport modelling and XPS fitting, proving to be a powerful tool in the determination of the likely defect species and in understanding the charge state of said defect which directly relates to the transport modelling. It is also worth reiterating that the effects of plasmon losses in FTO as seen in XPS analysis have been scarcely touched upon in the literature. This could easily lead to the misassignment of spectral features.

From the above we can infer that the carrier density of these FTO films is heavily compensated, with the measured free carrier concentration being about one third of the total fluorine incorporation - for every two substitutional F donor there is approximately one interstitial F acceptor, resulting in roughly one free electron for every three F atoms. Or, more precisely, for our range of substitutional to interstitial F 1s area ratios of 0.47 to 0.53, there

are on average between 2.9 and 3.1 F atoms per free electron. Indeed, this is supported by comparing the F contents estimated from XPS with the free electron densities from Hall effect. As discussed in the methods section below, from XPS we estimate that the F content in the FTO films is in the range 0.7-1.7 atomic % (but with considerable uncertainty in the absolute atomic % values as discussed in the methods section). Considering the atomic density of SnO_2 of 8.4×10^{22} cm^{-3}, this corresponds to F concentrations in the range of around 5.9×10^{20} to 1.4×10^{21} cm^{-3}. Comparing this to the Hall carrier concentration range of 1.8–5.5×10^{20} cm^{-3} reveals between 2.5 and 3.3 F atoms per free electron in agreement with the expectation of the F concentration being about three times the carrier density.

To provide additional evidence of this finding with greater accuracy than XPS and without the limitations of the surface sensitivity of XPS, time of flight (ToF) secondary ion mass spectrometry (SIMS) was used. Information on the specific SIMS system used and experimental procedure is in the supporting information, along with a plot of F atomic concentration versus sputter depth for F-concentrations in FTO samples and an F-ion implanted SnO_2 standard, seen in Figure S7. F-ion implanted standards were used in combination with profilometry (for depth calibration) to obtain the atomic concentration of F. SIMS was performed on typical FTO samples with a Hall carrier concentration of $n = 4.05 \times 10^{20}$cm^{-3} and $n = 4.27 \times 10^{20}$ cm^{-3} (corresponding to the sample seen in figure 6). The depth-averaged total concentration of F determined by calibrated SIMS was found to be [F] = (1.08±0.11) $\times 10^{21}$ cm^{-3} and [F] = (1.06±0.11) $\times 10^{21}$ cm^{-3} respectively. This indicates about 2.5-2.7 F atoms per free electron. This confirms that the total F content is approximately 3 times greater than the free electron density, n.

This additional F content has the effect of reducing the achievable mobility from a maximum of around $\mu_{theory} = 120$ cm$^2/V \cdot s$ to under $\mu_{experiment} = 40$ cm$^2/V \cdot s$ for a carrier density of $n \sim 4 \times 10^{20}$ cm^{-3}. This has strong implications for the material performance. With this in mind we demonstrate that FTO possesses intrinsic limitations on its mobility and carrier density due to this self compensation. Although these materials display excel-

lent transparency and conductivity properties, in order to improve industrial-scale TCOs, alternative dopants need to be identified and their defect chemistry explored in order to find dopants which do not exhibit this self-compensating phenomenon inherent to fluorine doping of SnO_2. One example of such a novel dopant is Mo in In_2O_3 which gives higher mobilities than Sn in In_2O_3 (see Ref. 77). Another example is Ta doping of SnO_2, where for films grown by pulsed laser deposition, mobilities as high as 83 $cm^2/V \cdot s$ have been reported for carrier densities of around 3 $\times 10^{20}$ cm^{-3}.[78] Such values are consistent with the transport modelling for the uncompensated case shown in Fig. 1, but have yet to be realised using a scalable deposition method. It is also noted that the mobility of molecular-beam epitaxy-grown Sb-doped SnO_2 with free electron density of 2.6 $\times$ 10^{20} cm^{-3} is limited to 35 $cm^2/V \cdot s$ even though calibrated SIMS indicates an Sb concentration of 2.8 $\times$ 10^{20} cm^{-3}, suggesting negligible compensation from Sb-related defects.[79] For the Sb-doped case, other mobility-limiting mechanisms may be present, such as hybridization of Sb-orbitals with the Sn-dominated conduction band states, leading to increase electron effective mass and reduced mobility.

Conclusion

Heavily n-type fluorine-doped tin dioxide ($n > 1 \times 10^{20}$ cm^{-3}) deposited on soda-lime glass via APCVD has been shown to exhibit inherent self-compensation, limiting the achievable free electron density, mobility and resulting conductivity. Modelling of mobility versus carrier density data from Hall effect measurements indicates ionized impurity scattering dominates and the mobility is limited to <40 $cm^2/V{\cdot}s$ by the presence of acceptors, with a compensation ratio of $K = 0.48$ as determined via Hall effect measurements. Density functional theory formation energy calculations determined interstitial fluorine in the -1 charge state to be the lowest formation energy acceptor defect for degenerately doped FTO. Core-level XPS measurements and analysis were performed on FTO, including paying particular attention

to the modelling of plasmon loss components of core level lines which result from energy loss to the collective excitations of free carriers in degenerately-doped semiconductors. A high binding-energy shoulder component was found in the F 1s core level-region and attributed to interstitial fluorine, F_i. This component has half the intensity of that due to substitutional donor fluorine, F_O, consistent with the determined compensation ratio. This quantitative connection between fluorine chemical analysis and transport modelling has not previously been made. Hence, we have provided new evidence of fluorine interstitial as the defect responsible for FTO falling well short of the theoretical ionized impurity scattering-limited mobility of >100 $cm^2/V{\cdot}s$. Quantitative analysis on F concentrations of samples made through Hall effect, XPS and SIMS provides further proof of compensation in FTO.

Experimental and Theoretical Methods

Fluorine-doped tin dioxide (FTO) thin films deposited on glass by APCVD were obtained from NSG Group. Samples consisted of a multi-layer structure with an undoped SnO_2 layer ∼25 nm deposited directly on the glass substrate providing a rough surface for the subsequent layers to adhere to. A SiO_2 layer follows of thickness ∼ 25 nm acting as a sodium diffusion barrier, and finally the electrically active F:SnO_2 layer is deposited. The tetragonal rutile structure associated with the SnO_2 was confirmed via x-ray diffraction (see Figure S5 in supporting information). The samples are polycrystalline in nature and no impurity phases were present. Samples were prepared for measurement by mechanically cleaning the surface with laboratory wipes and isopropyl alcohol to remove large particulates, as well as being treated in an ultrasonic bath submerged in diluted surface cleaner (decon 90 surface cleaning agent) and then isopropyl alcohol, and rinsed in deionized water.

Time-of-flight secondary ion mass spectrometry (SIMS) combined with profilometry allowed the thickness of the FTO films to be determined. Film thickness of the FTO layers ranged from 300 to 750 nm. Fluorine concentrations in the films were determined from

XPS peak areas of the main core levels of the constituent elements, taking into account the atomic sensitivity factors (ASF) provided by Moulder *et al.*,[59] which ensure measured peak areas are corrected to account for photoionization cross sections. It should be noted that the ASF also depend on some factors specific to the measurement instrument used such as the analyser transmission function. The ASF taken from Moulder *et al.* are not specific to our XPS system and so the uncertainty associated with the determination of compositions can be considered sizeable. The fluorine concentration of the samples varied from around 0.7% (atomic percentage) to 1.7%.

Hall effect measurements were performed using the standard van der Pauw configuration at a field strength of 0.8 T to determine the free carrier concentration (n) and transport mobility (μ) of FTO samples. Measurements were performed at room temperature on the samples, all of which displayed n-type conductivity. The measured free carrier concentrations across the sample range varied from $(1.81 \pm 0.01) \times 10^{20}$ cm^{-3} to $(5.48 \pm 0.04) \times 10^{20}$ cm^{-3} and electron mobilities varied from 27.3 ± 0.2 cm^2/V·s to 38.2 ± 0.1 cm^2/V·s. Samples which displayed high carrier concentrations and low mobilities corresponded to those of high fluorine content. Temperature dependent Hall effect was also performed on some samples, with sample temperature being varied from 10 to 300 K ($\pm$0.5 K) (see Figure S1 in supporting information).

High resolution XPS measurements were performed using a SPECS monochromatic Al Kα (hv = 1486.6 eV) X-ray source operated at 300 W. Photoelectrons were analysed using a PSP Vacuum Technology hemispherical electron-energy analyser, with mean-radius of 120 mm operated at a pass energy of 10eV. The spectrometer was calibrated using a polycrystalline silver foil which had been Ar^+ sputtered to achieve a clean surface. The silver $3d_{5/2}$ and Fermi edge were measured for energy position and peak width calibration. For more information on the calibration process and estimated uncertainties of peak measurements made with this spectrometer see Ref. 80. All core level positions were referenced to the Fermi level of the FTO. While under ultra-high vacuum conditions, further surface

treatment was performed to remove surface contaminants. This was done via Ar^+ ion bombardment while monitoring the C 1s peak and Sn 3d peaks at regular intervals. Sn $3d_{5/2}$ to C 1s peak ratios were compared between sputter cycles in order to assess the level of surface cleanliness achieved. It should be noted that due to the small quantity of fluorine present in the samples and the relatively low cross section for photoionisation of F 1s photoelectrons, obtaining reasonable signal-to-noise on the fluorine 1s region takes 10-50 hours of data acquisition. This is consistent with what has been seen previously.[13,75,76]

Infrared (IR) reflectance measurements were performed using a Bruker Vertex 70v Fourier-transform infrared spectrometer at 11° angle of incidence (with respect to the normal of the sample surface). A CaF_2 beam splitter and DLaTGS detector were used. Spectra were recorded over an energy range of 0.10 to 0.75 eV in order to completely encompass the plasma resonance cut-off. FTIR measurements were performed under vacuum (∼2 mbar) to minimise the effect of atmospheric water vapour and carbon dioxide vibrational modes on the recorded spectra. The reflectance was simulated using the transfer matrix method.[81] The simulation accounted for both s and p-polarized reflectance, considering a five layer (vacuum/F:SnO_2/SiO_2/SnO_2/soda-lime glass) stratified medium, assuming complete incoherence in the thick glass substrate. The simulation uses a two-oscillator expression for the dielectric function to allow for determination of optical parameters. Transmittance was measured with a Shimadzu UV-Vis-IR 3700 spectrophotometer over an energy range of 1 to 5 eV.

Computational Methodology

Ab-initio calculations were performed using density functional theory (DFT) implemented using the periodic code, VASP.[82–85] The projector-augmented wave method (PAW)[86,87] was used to describe the interaction between the core electrons (Sn[Kr], O[He], F[He]) and the valence electrons. The hybrid functional PBE0 developed by Adamo and Barone[88,89] was used in order to combat the *self-interaction error* and thus allow for an accurate description

of the band gap of SnO_2. Hybrid functionals have consistently shown to provide improved calculations of both geometry and electronic structure,[58,90–92,92–96] and PBE0 has been shown to predict these properties for tin based TCOs with a high degree of accuracy.[53,54,97–102] PBE0 incorporates 25% of exact Fock exchange to the PBE (Perdew Burke and Ernzerhoff)[103] formalism.

The intrinsic defects and extrinsic dopants were simulated using a $2 \times 2 \times 3$ supercell containing 72 atoms together with a Γ-centred $2 \times 2 \times 2$ k-point mesh and a 400 eV plane wave energy cutoff. All the defect calculations were spin-polarised. The individual systems were deemed to be converged when the forces on all the atoms were less than 0.01 eV/ atom.

Defect Formalism

For a charge state q the formation energy of each defect is defined by

$$\Delta H_f(D,q) = (E^{D,q} - E^H) + \sum_i n_i(E_i + \mu_i) + q(E_{Fermi} + \epsilon^H_{VBM}) + E_{corr}[q] \qquad (1)$$

where E^H is the energy of the host supercell and $E^{D,q}$ is the energy of the supercell containing the defect in charge state q. E_i corresponds to the elemental reference energy ($Sn_{(s)}$, $O_{2(g)}$ and $F_{(g)}$) and the associated chemical potential is denoted μ_i. n refers to the number of electrons added to or taken away from an external resevoir.[104] In this work the Fermi level ranges from the valence band maximum (VBM) (where ϵ^H_{VBM} denotes the eigenvalue of the VBM in the host material) to $\sim$ 3.4 eV above the conduction band minimum (CBM). Finally, a correction term is applied to allow for 'finite size effects' and is shown by E_{corr}. This correction term encompasses three seperate corrections; firstly, there is the *image charge correction* which, due to the long ranged nature of the Coulomb interaction,[105,106] corrects for the interaction of the charged defect and its own periodic images. This is implemented using the correction scheme formalised by Hine and Murphy[107] which utilises the *dielectric tensor*. Secondly a simple *potential alignment* is applied which aligns the VBM of the defective supercell to that of the host supercell and lastly a *band filling* correction created by Lany and Zunger[108,109]

is applied to account for the high defect concentrations present in supercells.

Thermodynamic Limits

The chemical potentials (μ_i) can reflect the equilibrium growth conditions which can be varied to simulate the experimental partial pressures defining the conditions of n and p-type defect formation. This is all relative to the calculated enthalpy of the host material

$$\mu_{\mathrm{Sn}} + 2\mu_{\mathrm{O}} = \Delta H_f^{\mathrm{SnO_2}} = -5.27\,\mathrm{eV} \tag{2}$$

The experimentally determined standard enthalpy of formation for SnO_2 is -5.98 eV,[110] which is in reasonable agreement with our calculated value at 0 K. Our calculations allow for the determination of two growth conditions, the *Sn-rich/O-poor* limit which typically favours the formation of n-type defects which is determined by the formation of metallic Sn.

$$\Delta\mu_{\mathrm{Sn}} = 0; \Delta\mu_{\mathrm{O}} = -2.64\,\mathrm{eV} \tag{3}$$

Likewise for p-type defect favourable formation conditions, *Sn-poor/O-rich*, is limited by the formation of O_2 gas.

$$\Delta\mu_{\mathrm{O}} = 0; \Delta\mu_{\mathrm{Sn}} = -5.27\,\mathrm{eV} \tag{4}$$

The solubilities of the F species are limited by the formation of the secondary phase, SnF_4

$$\mu_{\mathrm{Sn}} + 4\mu_{\mathrm{F}} = \Delta H_f^{\mathrm{SnF_4}} = -12.43\,\mathrm{eV} \tag{5}$$

where $\Delta\mu_{\mathrm{F}}$ can be calculated to be -1.79 eV and -3.11 eV under *Sn-poor/O-rich* and *Sn-rich/O-poor* conditions respectively. (The experimentally defined standard enthalpy of formation for SnF_4 is -12.14 eV.[111])

The ionisation levels or thermodynamic transition levels are displayed in Figure 2 which for a given defect display the Fermi-level position where a given defect changes from charge state q to q' which is calculated by

$$\epsilon_D \frac{q}{q'} = \frac{\Delta H_f(D,q) - \Delta H_f(D,q')}{q' - q} \tag{6}$$

These transition levels can be observed using techniques such as deep level transient spectroscopy (DLTS) as the final charge state can relax to its equilibrium configuration after the transition.

Dependance on Oxygen Partial Pressure and Temperature

The dependance of μ_{O} on the oxygen partial pressure and temperature can be determined using the equation outlined by Reuter and Scheffler[112]

$$\mu_{\mathrm{O}}(T,p^0) = \frac{1}{2}[H(T,p^0,\mathrm{O}_2) - H(0K,p^0,\mathrm{O}_2)] - \frac{1}{2}T[S(T,p^0,\mathrm{O}_2) - S(0K,p^0,\mathrm{O}_2)] \tag{7}$$

where *T, H* and *S* are temperature, enthalpy and entropy respectively and $p^0 = 1\,\mathrm{atm}$ (with reference to a zero state ; $\mu_{\mathrm{O}}(0\mathrm{K},p^0)=\frac{1}{2}E^{total}_{\mathrm{O}_2} = 0$).[113,114] The temperatures used for the APCVD deposition in this study is ∼900 K meaning we can determine μ_{O} using data from thermochemical tables[115] giving

$$\mu_{\mathrm{O}}(T,p^0) = -0.97\,\mathrm{eV} \tag{8}$$

Supporting Information

Supplementary data is available at the Wiley Online Library [Insert reference containing DOI here], where the following are presented: Hall effect data of the temperature-dependence of

free carrier concentration and mobility; experimental resistivity versus carrier density with transport modelling; XPS data and curve fitting for an as-entered FTO sample prior to Ar^+ ion bombardment; ratio of interstitial to substitutional F peak areas determined by XPS for several FTO samples with different carrier concentrations; A typical x-ray diffraction plot obtained for FTO indexed with calculated diffraction peak positions; A typical transmission spectra for an FTO sample; Calibrated SIMS measurement of FTO and a fluorine-implanted standard; and a comparison of F 1s peak positions from this work and previous studies of F-doped SnO_2 and TiO_2.

Acknowledgement

This work was supported by the Engineering and Physical Sciences Research Council (EPSRC) [grant numbers EP/N01572X/1, EP/N015800/1]. JENS acknowledges studentship support from the EPSRC Centre for Doctoral Training in New and Sustainable Photovoltaics [grant number EP/L01551X/1]. TJW's studentship is funded by the EPSRC Doctoral Training Partnership [grant numbers EP/L505018/1, and EP/K503095/1]. This work made use of the ARCHER UK National Supercomputing Service (http://www.archer.ac.uk) via our membership of the UK's HEC Materials Chemistry Consortium, which is funded by EPSRC [EP/L000202]. The UCL Legion and Grace HPC Facilities (Legion@UCL and Grace@UCL) were also used in the completion of this work. DOS and TDV acknowledge membership of the Materials Design Network.

References

(1) Hosono, H. *Thin Solid Films* **2007**, *515*, 6000–6014.

(2) Stadler, A. *Materials* **2012**, *5*, 661–683.

(3) Coutts, T. J.; Mason, T. O.; Perkins, J. D.; Ginley, D. S. Transparent Conducting

Oxides : Status and Opportunities in Basic Research. Presented at the 195th Meeting of the Electrochemical Society. Seattle, Washington, 1999; pp 274–288.

(4) Gordon, R. G. *MRS Bulletin* **2000**, *25*, 52–57.

(5) Ellmer, K. *Nature Photonics* **2012**, *6*, 808–816.

(6) Ginley, D. S.; Bright, C. *MRS Bulletin* **2000**, *25*, 15–18.

(7) Kolmakov, A.; Zhang, Y.; Cheng, G.; Moskovits, M. *Advanced Materials* **2003**, *15*, 997–1000.

(8) Ginley, D. S.; Hosono, H.; Paine, D. C. *Handbook of Transparent Conductors*; Springer: New York, 2011.

(9) Baek, W.-H.; Choi, M.; Yoon, T.-S.; Lee, H. H.; Kim, Y.-S. *Applied Physics Letters* **2010**, *96*, 133506.

(10) Elangovan, E.; Ramamurthi, K. *Applied Surface Science* **2005**, *249*, 183–196.

(11) Agashe, C.; Major, S. S. *Journal of Materials Science* **1996**, *31*, 2965–2969.

(12) Rey, G.; Ternon, C.; Modreanu, M.; Mescot, X.; Consonni, V.; Bellet, D. *Journal of Applied Physics* **2013**, *114*, 183713.

(13) Park, J. H.; Byun, D. J.; Lee, J. K. *Journal of Electroceramics* **2009**, *23*, 506–511.

(14) Kim, H.; Auyeung, R. C. Y.; Piqué, A. *Thin Solid Films* **2008**, *516*, 5052–5056.

(15) Geoffroy, C.; Campet, G.; Menil, F.; Portier, J.; Salardenne, J.; Couturier, G. *Active and Passive Electronic Components* **1991**, *14*, 111–118.

(16) Bhachu, D. S.; Waugh, M. R.; Zeissler, K.; Branford, W. R.; Parkin, I. P. *Chemistry - A European Journal* **2011**, *17*, 11613–11621.

(17) Reimann, K.; Steube, M. *Solid State Communications* **1998**, *105*, 649–652.

(18) Arlinghaus, F. J. *Journal of Physics and Chemistry of Solids* **1974**, *35*, 931–935.

(19) Rakhshani, A. E.; Makdisi, Y.; Ramazaniyan, H. A. *Journal of Applied Physics* **1998**, *83*, 1049–1057.

(20) Noor, N.; Chew, C. K. T.; Bhachu, D. S.; Waugh, M. R.; Carmalt, C. J.; Parkin, I. P. *J. Mater. Chem. C* **2015**, *3*, 9359–9368.

(21) Xu, J.; Huang, S.; Wang, Z. *Solid State Communications* **2009**, *149*, 527–531.

(22) Noor, N.; Parkin, I. P. *J. Mater. Chem. C* **2013**, *1*, 984–996.

(23) Shanthi, E.; Banerjee, A.; Dutta, V.; Chopra, K. L. *Journal of Applied Physics* **1982**, *53*, 1615–1621.

(24) Granqvist, C. G. *Solar Energy Materials and Solar Cells* **2007**, *91*, 1529–1598.

(25) Porch, A.; Morgan, D. V.; Perks, R. M.; Jones, M. O.; Edwards, P. P. *Journal of Applied Physics* **2004**, *95*, 4734–4737.

(26) Edwards, P. P.; Porch, A.; Jones, M. O.; Morgan, D. V.; Perks, R. M. *Dalton Transactions* **2004**, 2995–3002.

(27) Acosta, D. R.; Zironi, E. P.; Montoya, E.; Estrada, W. *Thin Solid Films* **1996**, *288*, 1–7.

(28) Fantini, M.; Torriani, I. *Thin Solid Films* **1986**, *138*, 255–265.

(29) Suffner, J.; Ágoston, P.; Kling, J.; Hahn, H. *Journal of Nanoparticle Research* **2010**, *12*, 2579–2588.

(30) Thangaraju, B. *Thin Solid Films* **2002**, *402*, 71–78.

(31) Bae, J. W.; Lee, S. W.; Yeom, G. Y. *Journal of The Electrochemical Society* **2007**, *154*, D34.

(32) Canestraro, C. D.; Oliveira, M. M.; Valaski, R.; da Silva, M. V. S.; David, D. G. F.; Pepe, I.; Silva, a. F. D.; Roman, L. S.; Persson, C. *Applied Surface Science* **2008**, *255*, 1874–1879.

(33) Chinnappa, L.; Ravichandran, K.; Saravanakumar, K.; Muruganantham, G.; Sakthivel, B. *Journal of Materials Science: Materials in Electronics* **2011**, *22*, 1827–1834.

(34) Ellmer, K. *Journal of Physics D: Applied Physics* **2001**, *34*, 3097–3108.

(35) Look, D. C.; Leedy, K. D.; Vines, L.; Svensson, B. G.; Zubiaga, A.; Tuomisto, F.; Doutt, D. R.; Brillson, L. J. *Physical Review B* **2011**, *84*, 115202.

(36) Brooks, H. *Advances in Electronics and Electron Physics* **1955**, *7*, 85–182.

(37) Look, D. C.; Stutz, C. E.; Molnar, R. J.; Saarinen, K.; Liliental-Weber, Z. *Solid State Communications* **2001**, *117*, 571–575.

(38) Fonstad, C. G.; Rediker, R. H. *Journal of Applied Physics* **1971**, *42*, 2911–2918.

(39) Bardeen, J.; Shockley, W. *Physical Review* **1950**, *80*, 72–80.

(40) Low, F. E.; Pines, D. *Physical Review* **1955**, *98*, 414–418.

(41) Frohlich, H.; Mott, N. F. *Proceedings of the Royal Society A: Mathematical, Physical and Engineering Sciences* **1939**, *171*, 496–504.

(42) Howarth, D. J.; Sondheimer, E. H. *Proceedings of the Royal Society A: Mathematical, Physical and Engineering Sciences* **1953**, *219*, 53–74.

(43) Bruneaux, J.; Cachet, H.; Froment, M.; Messad, A. *Thin Solid Films* **1991**, *197*, 129–142.

(44) Seto, J. Y. W. *Journal of Applied Physics* **1975**, *46*, 5247–5254.

(45) Button, K. J.; Fonstad, C. G.; Dreybrodt, W. *Physical Review B* **1971**, *4*, 4539–4542.

(46) Jarzebski, Z. M. *Journal of The Electrochemical Society* **1976**, *123*, 333C.

(47) Pisarkiewicz, T.; Kolodziej, A. *Physica Status Solidi (B)* **1990**, *158*, K5.

(48) Martínez, A. I.; Huerta, L.; de León, J. M. O.-R.; Acosta, D.; Malik, O.; Aguilar, M. *Journal of Physics D: Applied Physics* **2006**, *39*, 5091–5096.

(49) Haitjema, H.; Elich, J.; Hoogendoorn, C. J. *Solar Energy Materials* **1989**, *18*, 283–297.

(50) Look, D. C.; Leedy, K. D.; Tomich, D. H.; Bayraktaroglu, B. *Applied Physics Letters* **2010**, *96*, 062102.

(51) Rauch, C.; Tuomisto, F.; King, P. D. C.; Veal, T. D.; Lu, H.; Schaff, W. J. **2012**, *101*, 011903.

(52) Singh, A. K.; Janotti, A.; Scheffler, M.; Van de Walle, C. G. *Physical Review Letters* **2008**, *101*, 055502.

(53) Ágoston, P.; Körber, C.; Klein, A.; Puska, M. J.; Nieminen, R. M.; Albe, K. *Journal of Applied Physics* **2010**, *108*, 053511.

(54) Ágoston, P.; Albe, K.; Nieminen, R. M.; Puska, M. J. *Physical Review Letters* **2009**, *103*, 245501.

(55) King, P. D. C.; Veal, T. D. *Journal of Physics: Condensed Matter* **2011**, *23*, 334214 and references therein.

(56) Makkonen, I.; Korhonen, E.; Prozheeva, V.; Tuomisto, F. *Journal of Physics: Condensed Matter* **2016**, *28*, 224002.

(57) Canestraro, C. D.; Roman, L. S.; Persson, C. *Thin Solid Films* **2009**, *517*, 6301–6304.

(58) Kafizas, A.; Noor, N.; Carmichael, P.; Scanlon, D. O.; Carmalt, C. J.; Parkin, I. P. *Advanced Functional Materials* **2013**, *24*, 1758–1771.

(59) Moulder, J. F.; Stickle, W. F.; Sobol, P. E.; Bomben, K. D. In *Handbook of X-ray Photoelectron Spectroscopy*; Chastain, J., King, R., Eds.; Physical Electronics, Division, Perkin-Elmer Corporation: Eden Prairie, Minnesota, USA, 1992; p 261.

(60) Ferraria, A. M.; Lopes da Silva, J. D.; Botelho do Rego, A. M. *Polymer* **2003**, *44*, 7241–7249.

(61) Sleigh, C.; Pijpers, A.; Jaspers, A.; Coussens, B.; Meier, R. J. *Journal of Electron Spectroscopy and Related Phenomena* **1996**, *77*, 41–57.

(62) Biesinger, M. C.; Payne, B. P.; Grosvenor, A. P.; Lau, L. W. M.; Gerson, A. R.; Smart, R. S. C. *Applied Surface Science* **2011**, *257*, 2717–2730.

(63) Egdell, R. G.; Rebane, J.; Walker, T.; Law, D. *Physical Review B* **1999**, *59*, 1792–1799.

(64) Egdell, R.; Walker, T.; Beamson, G. *Journal of Electron Spectroscopy and Related Phenomena* **2003**, *128*, 59–66.

(65) Kotani, A.; Toyozawa, Y. *Journal of the Physical Society of Japan* **1974**, *37*, 912–919.

(66) Payne, D. J.; Egdell, R. G.; Law, D. S. L.; Glans, P.-A.; Learmonth, T.; Smith, K. E.; Guo, J.; Walsh, A.; Watson, G. W. *J. Mater. Chem.* **2007**, *17*, 267–277.

(67) Weidner, M. Fermi Level Determination in Tin Oxide by Photoelectron Spectroscopy - Relation to Optoelectronic Properties; Band Bending at Surfaces and Interfaces; Modulation Doping. Ph.D. thesis, TU Darmstadt, 2015.

(68) Shirley, D. A. *Physical Review B* **1972**, *5*, 4709–4714.

(69) Cox, P. A.; Egdell, R. G.; Harding, C.; Patterson, W. R.; Tavener, P. J. *Surface Science* **1982**, *123*, 179–203.

(70) Veal, T. D.; McConville, C. F. *Physical Review B* **2001**, *64*, 85311.

(71) Vasheghani Farahani, S. K.; Veal, T. D.; King, P. D. C.; Zúñiga-Pérez, J.; Muñoz-Sanjosé, V.; McConville, C. F. *Journal of Applied Physics* **2011**, *109*, 073712.

(72) Taylor, J. A.; Lancaster, G. M.; Rabalais, J. W. *Journal of Electron Spectroscopy and Related Phenomena* **1978**, *13*, 435–444.

(73) Willemen, H.; Van De Vondel, D.; Van Der Kelen, G. *Inorganica Chimica Acta* **1979**, *34*, 175–180.

(74) Wu, S.; Yuan, S.; Shi, L.; Zhao, Y.; Fang, J. *Journal of Colloid and Interface Science* **2010**, *346*, 12–16.

(75) Pandey, R.; Cho, S.; Hwang, D.; Choi, W. *Current Applied Physics* **2014**, *14*, 850–855.

(76) Pan, Z.; Zhang, P.; Tian, X.; Cheng, G.; Xie, Y.; Zhang, H.; Zeng, X.; Xiao, C.; Hu, G.; Wei, Z. *Journal of Alloys and Compounds* **2013**, *576*, 31–37.

(77) Bhachu, D. S.; Scanlon, D. O.; Sankar, G.; Veal, T. D.; Egdell, R. G.; Cibin, G.; Dent, A. J.; Knapp, C. E.; Carmalt, C. J.; Parkin, I. P. *Chemistry of Materials* **2015**, *27*, 2788–2796.

(78) Nakao, S.; Yamada, N.; Hitosugi, T.; Hirose, Y.; Shimada, T.; Hasegawa, T. *Applied Physics Express* **2010**, *3*, 031102.

(79) Feneberg, M.; Lidig, C.; Lange, K.; White, M. E.; Tsai, M. Y.; Speck, J. S.; Bierwagen, O.; Goldhahn, R. *Physica Status Solidi (A) Applications and Materials Science* **2014**, *211*, 82–86.

(80) Whittles, T. J.; Burton, L. A.; Skelton, J. M.; Walsh, A.; Veal, T. D.; Dhanak, V. R. *Chemistry of Materials* **2016**, *28*, 3718–3726.

(81) Katsidis, C. C.; Siapkas, D. I. *Applied Optics* **2002**, *41*, 3978–3987.

(82) Kresse, G.; Hafner, J. *Physical Review B* **1993**, *47*, 558–561.

(83) Kresse, G.; Hafner, J. *Physical Review B* **1994**, *49*, 14251–14269.

(84) Kresse, G.; Furthmüller, J. *Physical Review B* **1996**, *54*, 11169–11186.

(85) Kresse, G.; Furthmüller, J. *Computational Materials Science* **1996**, *6*, 15–50.

(86) Blöchl, P. E. *Physical Review B* **1994**, *50*, 17953–17979.

(87) Kresse, G.; Joubert, D. *Physical Review B* **1999**, *59*, 1758–1775.

(88) Adamo, C.; Barone, V. *The Journal of Chemical Physics* **1999**, *110*, 6158–6170.

(89) Paier, J.; Hirschl, R.; Marsman, M.; Kresse, G. *The Journal of Chemical Physics* **2005**, *122*, 234102.

(90) Williamson, B. A. D.; Buckeridge, J.; Brown, J.; Ansbro, S.; Palgrave, R. G.; Scanlon, D. O. *Chemistry of Materials* **2016**, DOI: 10.1021/acs.chemmater.6b03306.

(91) Marchand, P.; Sathasivam, S.; Williamson, B. A. D.; Pugh, D.; Bawaked, S. M.; Basahel, S. N.; Obaid, A. Y.; Scanlon, D. O.; Parkin, I. P.; Carmalt, C. J. *J. Mater. Chem. C* **2016**, *4*, 6761–6768.

(92) Sathasivam, S.; Williamson, B. A. D.; Kafizas, A.; Althabaiti, S. A.; Obaid, A. Y.; Basahel, S. N.; Scanlon, D. O.; Carmalt, C. J.; Parkin, I. P. *The Journal of Physical Chemistry C* **2017**, *121*, 202–210.

(93) Oba, F.; Togo, A.; Tanaka, I.; Paier, J.; Kresse, G. *Physical Review B* **2008**, *77*, 245202.

(94) Chen, H.; Dawson, J. A. *The Journal of Physical Chemistry C* **2015**, *119*, 15890–15895.

(95) Bhachu, D. S.; Sathasivam, S.; Sankar, G.; Scanlon, D. O.; Cibin, G.; Carmalt, C. J.; Parkin, I. P.; Watson, G. W.; Bawaked, S. M.; Obaid, A. Y.; Al-Thabaiti, S.; Basahel, S. N. *Advanced Functional Materials* **2014**, *24*, 5075–5085.

(96) Burbano, M.; Scanlon, D. O.; Watson, G. W. *Journal of the American Chemical Society* **2011**, *133*, 15065–15072.

(97) Scanlon, D. O.; Watson, G. W. *Journal of Materials Chemistry* **2012**, *22*, 25236–25245.

(98) Ganose, A. M.; Scanlon, D. O. *J. Mater. Chem. C* **2016**, *4*, 1467–1475.

(99) Vasheghani Farahani, S. K.; Veal, T. D.; Mudd, J. J.; Scanlon, D. O.; Watson, G. W.; Bierwagen, O.; White, M. E.; Speck, J. S.; McConville, C. F. *Physical Review B* **2014**, *90*, 155413.

(100) Lebens-Higgins, Z.; Scanlon, D. O.; Paik, H.; Sallis, S.; Nie, Y.; Uchida, M.; Quackenbush, N. F.; Wahila, M. J.; Sterbinsky, G. E.; Arena, D. A.; Woicik, J. C.; Schlom, D. G.; Piper, L. F. J. *Physical Review Letters* **2016**, *116*, 027602.

(101) Sallis, S.; Scanlon, D. O.; Chae, S. C.; Quackenbush, N. F.; Fischer, D. A.; Woicik, J. C.; Guo, J.-H.; Cheong, S. W.; Piper, L. F. J. *Applied Physics Letters* **2013**, *103*, 42105.

(102) Scanlon, D. O. *Physical Review B* **2013**, *87*, 161201.

(103) Perdew, J. P.; Burke, K.; Ernzerhof, M. *Physical Review Letters* **1996**, *77*, 3865–3868.

(104) Van de Walle, C. G.; Neugebauer, J. *Journal of Applied Physics* **2004**, *95*, 3851–3879.

(105) Hine, N. D. M.; Frensch, K.; Foulkes, W. M. C.; Finnis, M. W. *Physical Review B* **2009**, *79*, 024112.

(106) Nieminen, R. M. *Modelling and Simulation in Materials Science and Engineering* **2009**, *17*, 84001.

(107) Murphy, S. T.; Hine, N. D. M. *Physical Review B* **2013**, *87*, 094111.

(108) Lany, S.; Zunger, A. *Physical Review B* **2008**, *78*, 235104.

(109) Freysoldt, C.; Neugebauer, J.; Van de Walle, C. G. *Physical Review Letters* **2009**, *102*, 016402.

(110) Lide, D. R. *CRC Handbook of Chemistry and Physics, 86th ed.*; CRC Press, Boca Raton, FL, 2005.

(111) Emeleus, H. J., Sharpe, A. G., Eds. *Advances in Inorganic Chemistry and Radiochemistry*; Academic Press, London, 1981.

(112) Reuter, K.; Scheffler, M. *Physical Review B* **2001**, *65*, 035406.

(113) Taylor, F. H.; Buckeridge, J.; Catlow, C. R. A. *Chemistry of Materials* **2016**, *28*, 8210–8220.

(114) Morgan, B. J.; Watson, G. W. *The Journal of Physical Chemistry C* **2010**, *114*, 2321–2328.

(115) Stull, D. R.; Prophet, H. *NSRDS-NBS (Book 37) ; National Bureau of Standards U.S: Washington, DC* **1971**,